RESEARCH ARTICLE

Check for updates

The Mössbauer effect using ^{57}Fe-ferrabisdicarbollide ([*o*-^{57}FESAN]$^−$): a glance into the potential of a low-dose approach for glioblastoma radiotherapy†

Ana B. Buades,[a] Laura C. J. Pereira, [b] Bruno J. C. Vieira, [b] Ana C. Cerdeira, [b] João C. Waerenborgh, [b] Teresa Pinheiro, [c] António P. A. Matos,[d] Catarina G. Pinto,[b] Joana F. Guerreiro, [b] Filipa Mendes, [b] Srecko Valic,[e] Francesc Teixidor, [a] Clara Viñas *[a] and Fernanda Marques *[b]

Although a variety of cancers are initially susceptible to chemotherapy, they eventually develop multi-drug resistance. To overcome this situation, more effective and selective treatments are necessary using anti-tumour agents that act in two or more ways and offer greater therapeutic benefits over single-mechanism entities. In this study, we report on treating cancer with Na[3,3′-^{57}Fe(1,2-C$_2$B$_9$H$_{11}$)$_2$], which offers the possibility of dual action (radiation–drug combinations) to improve the clinical benefits and reduce healthy tissue toxicity. An approach to evaluating the potential of [*o*-^{57}FESAN]$^−$ to treat glioblastoma using the Mössbauer effect is presented. As the therapeutic outcomes rely on the amount and distribution of [*o*-^{57}FESAN]$^−$ inside the cells, several studies, using magnetization, Mössbauer spectroscopy and nuclear microscopy techniques, were performed to ascertain the uptake of [*o*-^{57}FESAN]$^−$ in U87 glioblastoma cells. [*o*-^{57}FESAN]$^−$ was found to be within the cells; 29% of its uptake was in the nuclear fraction, which is a particularly desirable target, because the nucleus is the cell's control centre where DNA and the transcription machinery reside. Irradiation studies with 2D and 3D cellular models of U87 cells showed that the growth inhibition effect observed was more pronounced when [*o*-^{57}FESAN]$^−$ was used in combination with the Mössbauer effect in low total dose regimens, suggesting that this procedure either alone or as adjuvant may be useful for glioblastoma treatment.

Introduction

Cancer is a multifactorial disorder, resulting from the combined effect of genetic and environmental factors. Predictions indicate an increase of up to 21.6 million cases of cancer every year until 2030, making cancer the leading cause of death worldwide.

The hallmarks of cancer include independence from growth signals, non-response to signals that stop cell division, uncontrolled replication and the evasion of apoptosis. Mössbauer spectroscopy, based on the recoilless emission and absorption of gamma rays in solids, is a versatile technique that provides important information regarding the chemical, structural and magnetic properties of a material in many areas of science, such as Physics, Chemistry, and Biology.[1] The applications of Mössbauer spectroscopy in biomedical research have become established through at least fifty years of experience in this field.

For iron-containing coordination complexes, Mössbauer spectroscopy is effective in determining the iron oxidation state (Fe^{2+} and Fe^{3+}), as well as the electronic spin-state, coordination number and environment, effectively discriminating different iron sites.

Iron is an ideal element for Mössbauer spectroscopy.[2] A source of ^{57}Co ($t_{1/2}$ = 270 d) decays by electron capture (EC from the K-shell) to the 136 keV nuclear level of ^{57}Fe. This

[a]Institut de Ciència de Materials de Barcelona, Consejo Superior de Investigaciones Científicas, Campus Universitat Autònoma de Barcelona, 08193 Bellaterra, Spain. E-mail: clara@icmab.es
[b]Centro de Ciências e Tecnologias Nucleares/Departamento de Ciências e Energia Nucleares, Instituto Superior Técnico, Universidade de Lisboa, Estrada Nacional 10 (km 139.7), 2695-066 Bobadela LRS, Portugal. E-mail: fmarujo@ctn.tecnico.ulisboa.pt
[c]Instituto de Bioengenharia e Biociências, Departamento de Engenharia e Ciências Nucleares, Instituto Superior Técnico, Universidade de Lisboa, Av. Rovisco Pais 1, 1049-001 Lisboa, Portugal
[d]Centro de Investigação Interdisciplinar Egas Moniz, Campus Universitário, Quinta da Granja, Monte de Caparica, 2829-511 Caparica, Portugal
[e]Ruđer Bošković Institute, Bijenička 54, HR-10000 Zagreb, Croatia
†Electronic supplementary information (ESI) available. See DOI: 10.1039/d1qi01513c

1490 | *Inorg. Chem. Front.*, 2022, **9**, 1490–1503

This journal is © the Partner Organisations 2022

excited state decays to the ground state of ^{57}Fe (15%) to the 14.4 keV level (85%). The half-life of this level ($t_{1/2}$ *ca.* 100 ns) and the emission of the 14.4 keV photon are ideally suited for ^{57}Fe Mössbauer spectroscopy. A fraction of the emitted 14.4 keV photons is recoil free and can be absorbed by a ^{57}Fe nucleus in a sample. Since the Mössbauer effect is only observed in the ^{57}Fe nuclei, which account for 2% of natural Fe, the study of samples with very low Fe content requires enrichment of the ^{57}Fe isotope.

In fact, in biological systems, iron is by far one of the most structurally and relevant metal ions and ^{57}Fe Mössbauer spectroscopy has been very useful in the elucidation of the electronic structures of iron-containing biomolecules, the role of iron in living processes and pathological changes in living systems, organs and tissues.[3–6]

Radiation therapy (RT) is the most frequently used therapeutic option for the treatment of cancer but high doses of ionizing radiation are delivered to tumours since only a small fraction of the absorbed dose can damage cancer cells. Moreover, the efficacy of RT is limited by the resistance of tumours as well as by the toxicity to normal cells and tissues.[7] The use of radiosensitizers has been suggested as a promising option to overcome the adverse side effects of RT and make this treatment more effective without increasing the dose of radiation, which may be detrimental to normal tissues. The radiosensitizing effect of platinum(II) cisplatin, whose primary target in cells is DNA,[8] has encouraged the design of many other transition metal coordination complexes or organometallic complexes and their assessment as anticancer candidates.[9–11]

Mössbauer absorption represents a method of increasing the radiosensitivity of tumours in terms of orders of magnitude *via* selective energy deposition in cancer cells. The secondary radiation accompanying resonance absorption of Mössbauer radiation in ^{57}Fe nuclei may be able to produce a powerful local effect on biological tissues. After gamma ray absorption, the excited nucleus decay is accompanied by a cascade of Auger or low-energy (of the order of 1 keV) conversion electrons that have much higher biological efficiency than the primary quanta. Therefore, a targeted radiation cancer treatment is foreseen using a method based on the use of secondary radiation excited in a ^{57}Fe target by a Mössbauer source. Moreover, irradiated tumour cells preloaded with iron (^{57}Fe) compounds with resonant Mössbauer γ rays could result in DNA damage through the production of Auger electrons and X-rays. The DNA double-strand breaks are more efficiently produced by Auger electrons (1–10 eV) generated in proximity to DNA. The energy of these electrons is dissipated within a cell diameter and produces multiple double-strand DNA breaks. A single Auger event can be lethal to a cell and is comparable with more than 10^5 photon absorption events in conventional radiotherapy. ^{57}Fe(III)-Bleomycin, administered to malignant cells *in vitro* and *in vivo* and irradiated with resonant Mössbauer gamma rays (14.4 keV), causes ablation of the malignant cells, presumably by Auger cascade, with extremely small radiation doses, about 10^{-5} Gy. As a basis for com-

parison, a dose of about 5 Gy is necessary to achieve a similar effect with conventional radiotherapy.[12]

In the field of tumour pathology, as an alternative to or in support of conventional radiotherapy, cancer cell inactivation by Mössbauer effect could also have future applications. Patients with chronic myelogenous leukemia (CML) could benefit from this therapeutic modality. Experiments done with bone marrow cells collected from normal donors and K562 leukaemic cells demonstrated a growth inhibition effect after treatment with hematin and low-energy γ rays from a ^{57}Co Mössbauer source.[13] Thus, Mössbauer cancer therapy promises the advantages of selective radiation without systemic exposure of normal tissue, as well as higher killing effect per event secondary to the production of Auger electrons.

Radiotherapy is a common step during the treatment of glioblastoma multiforme (GBM), the most malignant brain cancer among adults and the second most common pediatric malignant tumour, with a very poor prognosis.[14] Rapid proliferation, high invasiveness and radiation resistance are the main reasons behind the poor therapeutic outcomes. To increase the effectiveness of radiotherapy, the use of radiosensitizers can enhance the radiosensitivity of tumour cells and reduce the radiation dose and the adverse effects on normal brain tissue. The radiosensitization effect of high-Z metals has been evaluated. It was found that the radiation dose was enhanced due to the generation of secondary X-rays, photoelectrons and Auger electrons with subsequently higher energy deposition in the cancer cells.[15] At present, the conventional radiotherapy sensitizers used in the clinic include 5-fluorouracil, temozolomide and platinum drugs, which can enhance the radiotherapy sensitivity of tumour cells through different mechanisms of action. However, these conventional radiotherapy sensitizers can cause many adverse side effects and acquired resistance.[16]

Recent studies have demonstrated that 3D hybrid organic–inorganic compounds, known as carboranes, can have a role in the development of novel small molecules for the treatment of various types of cancer.[17–21] The synthetic flexibility of carboranes, along with their rigid structure and chemical stability, makes them appealing moieties for their use in cancer drug development.[22,23] Although carborane-based drugs are yet to be approved for therapeutic purposes, many compounds have shown promising properties for biomedical applications, in particular for boron neutron capture therapy (BNCT).[24–30] In other biomedical fields, cobaltabis(dicarbollide) complexes known as [*o*-COSAN]$^-$ species have shown important selective HIV-1 protease inhibition activity and, if combined with specific biomolecules, could be promising for targeted therapy.[31]

A study by Mössbauer spectroscopy of intramolecular rotations and electronic states of Fe in the salt Cs[*o*-FESAN] and the zwitterion boron compound [Fe(8-(C$_2$H$_4$O)$_2$-1,2-C$_2$B$_9$H$_{10}$)(1′,2′-C$_2$B$_9$H$_{11}$)] was recently published.[32] In the present work, we aim to evaluate the potential of ^{57}Fe-ferrabis(dicarbollide), herein [*o*-^{57}FESAN]$^-$, as a radiosensitizer *via* the Mössbauer effect to treat glioblastoma. As the therapeutic

This journal is © the Partner Organisations 2022

Inorg. Chem. Front., 2022, **9**, 1490–1503 | **1491**

efficiency relies on the cellular amount and distribution of [o-^{57}FESAN]$^-$, we have evaluated quantitatively the net iron uptake in both GBM and normal astrocyte cell lines (U87 and rat astrocyte RA, respectively). Furthermore, the spatial subcellular distribution of iron has been measured with nuclear microscopy techniques, which rely on energetic ion beams focused to micrometre dimensions.[33] These techniques offer the distinct possibility of imaging the morphology of single cells with relatively high resolution and quantitating elemental distribution with high-sensitivity (μg g^{-1} range) in conditions close to those found *in vivo*, without the need for stains or contrast agents.[34] These possibilities are of the utmost importance for the preservation of the original physiological conditions to ensure realistic two-dimensional microanalysis in single cells, enabling Fe distribution to be visualized and its uptake quantified.

Experimental

Synthesis of Na[o-^{57}FESAN]

The first step was the synthesis of [NMe$_4$][o-^{57}FESAN] (see ESI†), which was achieved by the complexation reaction of the dicarbollide ligand ([7,8-C$_2$B$_9$H$_{11}$]$^{2-}$) with ^{57}FeCl$_2$ using a modified method[35] for the original synthesis by Hawthorne *et al.*[36] The sodium salt of the anionic [o-^{57}FESAN]$^-$ was obtained by means of the cationic exchange resin of its caesium salt as displayed in Scheme 1. The Na$^+$ salt was characterized by ^{1}H and ^{11}B NMR, EPR as well as by MALDI-TOF, as reported in the ESI.†

Paramagnetic properties of Na[o-FESAN]

As the anionic [o-FESAN]$^-$ complex is an $S = 1/2$ species, to assess the magnetic properties of the paramagnetic Na[o-FESAN], EPR measurements on Na[o-FESAN] were also run in the solid state and in acetone solution. The EPR spectra of the recently reported low-spin [NMe$_4$][o-FESAN] salt[37] and ferrocene were also run for comparison.

Magnetization and Mössbauer spectroscopy studies

Magnetic measurements of the parent ferrabis(dicarbollide), [o-^{57}FESANE]$^-$ anion, as well as of the U87 glioblastoma and RA cells exposed to [o-^{57}FESAN], were performed using a SQUID magnetometer S700X (Cryogenic Ltd) in the 4–300 K temperature range under fields of 0.1 T (iron compound) and 1 T (cell samples). Mössbauer spectra of parent Na[o-^{57}FESAN] and U87 and RA cells loaded with Na[o-^{57}FESAN] (300 μM, 6 h incubation) were collected at 80 K using a conventional constant acceleration spectrometer and a ^{57}Co (Rh) source. The velocity scale was calibrated with an α-Fe foil. The spectra were fitted to Lorentzian lines using a non-linear least-squares method.[38] The measurements run at 80 K were obtained with the samples immersed in He gas in a bath cryostat.

Irradiation studies

For cell irradiation with the ^{57}Co source, the velocity range of the spectrometer transducer was restricted to the Doppler frequencies where resonant γ-ray absorption was observed in the Mössbauer spectra of the cells. This procedure implies that the sample was permanently subjected to the γ-ray absorption *via* the Mössbauer effect during the irradiation time of ~2 h. The dose received by the sample due to all the γ- and X-rays emitted by the ^{57}Co source was ~0.4 mGy.

Biological studies

Cell viability assays. The glioblastoma cell line U87 (ATCC) and the rat astrocyte (RA) cell line (Sigma-Aldrich) were cultured in MEM (U87) containing GlutaMax-I supplemented with 10% FBS and in astrocyte medium (RA) (Gibco, ThermoFisher) at 37 °C in a humidified atmosphere of 5% CO$_2$ (Heraeus, Germany). Cells were seeded in 96-well plates at a density of 2×10^4 cells (U87) and 5×10^4 cells (RA) per well in 200 μL of culture medium and left to incubate overnight for optimal adherence. After careful removal of the medium, 200 μL of a dilution series of the Na[o-^{57}FESAN] compound (from a stock solution of 1 mM in medium) were added and

● C-H
● B-H
● ^{57}Fe
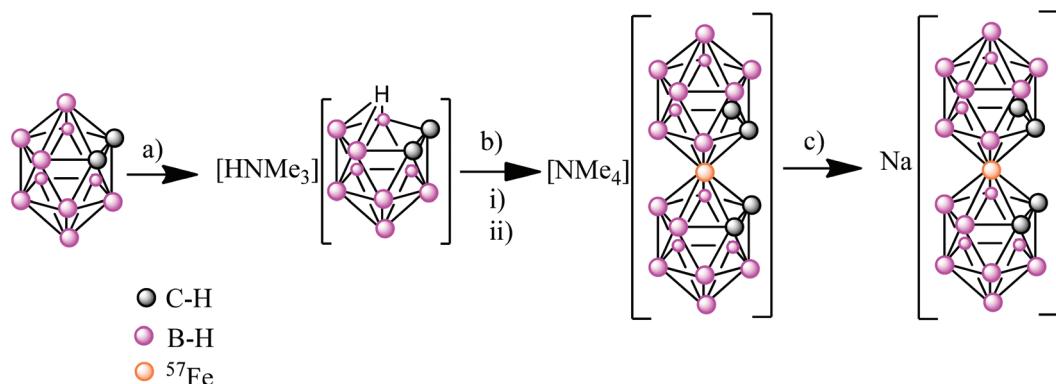
Scheme 1 Synthesis of Na[o-^{57}FESAN]. (a) Partial deboronation of the neutral *closo* 1,2-C$_2$B$_{10}$H$_{12}$. (b) Complexation reaction of the monoanionic *nido* [7,8-C$_2$B$_9$H$_{12}$]$^-$ ligand in two steps: (i) deprotonation reaction with K[t-BuO] in dry THF and (ii) complexation of the dianionic *nido* [7,8-C$_2$B$_9$H$_{11}$]$^{2-}$ with ^{57}FeCl$_2$ to obtain [3,3'-^{57}Fe(1,2-C$_2$B$_9$H$_{11}$)$_2$]$^-$ (abbreviated as [o-^{57}FESAN]$^-$) that was precipitated as a salt of [NMe$_4$]$^+$. (c) The Na$^+$ salt was obtained from the [NMe$_4$]$^+$ using cationic exchange resin.

1492 | *Inorg. Chem. Front.*, 2022, **9**, 1490–1503

This journal is © the Partner Organisations 2022

incubation was performed at 37 °C/5% CO_2 for 24 h. Cell viability was evaluated using the MTT assay as described in the literature.[39] The IC_{50} values were determined from dose–response curves using the GraphPad Prism software (*vs.* 5).

Analysis of cellular uptake of small anionic [*o*-⁵⁷FESAN]⁻ molecules. The concentration of Fe in U87 and RA cells was determined using particle-induced X-ray emission (PIXE) technique at the Van de Graaf accelerator of the Instituto Superior Técnico (IST). The cells were incubated with the Na[*o*-⁵⁷FESAN] at 50 μM for 24 h. Whole cells and nuclear fractions were analyzed. The cell pellets (total whole-cell fraction) were obtained by centrifugation after washing the cells with PBS to remove the culture medium. The cellular nuclear fraction was obtained as described,[40] incubating the cells after treatment for 15 min at 4 °C with an isotonic buffer containing 0.1% IGEPAL CA-630, followed by vortexing and centrifugation at 400g for 5 min. After centrifugation, the supernatant was removed and the harvested nuclei pellets were collected. Both fractions were freeze-dried and digested in nitric acid together with yttrium (Y) (100 mg l⁻¹) as an internal standard. The procedure combined ultrasound cycles and microwave-assisted acid digestion. The detailed methodology encompassing sample preparation, PIXE analysis, concentration calculation and quality control, was as previously described.[41,42] The elemental concentrations were obtained in μg per g (of dry material) and converted to μg per 10⁶ cells.

Imaging Fe distribution in U87 cells. U87 cells (5–6 × 10⁵ cells) were prepared for nuclear microscopy experiments by seeding the cells on silicon frames with 5 × 3 windows of 0.56 mm² covered with a 100 nm thick silicon nitride membrane (Silson Ltd, UK) in 6-well plates and incubated overnight. The silicon nitride windows were previously sterilized with UV light. Cells were incubated with Na[*o*-⁵⁷FESAN] for 24 h at 50 μM (a non-cytotoxic dose) at 37 °C in a 5% CO_2 incubator. After incubation, the medium was removed and the windows were washed with cold PBS. Samples were frozen at −80 °C and then dried in a cryostat at −25 °C for subsequent analysis as described elsewhere.[34] Nuclear microscopy analysis of single cells was carried out in a vacuum with a 2.0 MeV proton beam focused to 2 μm dimensions at the nuclear microprobe facility (Oxford Microbeams Ltd, UK) of IST.[33] By scanning the beam across the target cell on the silicon nitride window, several techniques can be used simultaneously, enabling visualization of the distribution of several elements and their localization and quantitation in the cell. Two-dimensional images of Fe and physiological elements in the cell can be obtained with PIXE, together with cell morphological details using scanning transmission ion microscopy (STIM) to obtain density maps and matrix composition estimation by analyzing the elastic backscattering spectrometry (EBS) spectra, which is necessary for PIXE mass normalization and to obtain quantitative data (μg per g dry material).[33] Images of whole U87 cells were taken with scan sizes ranging between 53 × 53 and 25 × 25 μm². Data acquisition, image processing and concentration calculation were performed using the OMDAQ-2007 system.[43]

3D spheroid cultures. U87 spheroids were prepared in Nunclon™ Sphera™ ultra-low-attachment 96U-well plates. Briefly, U87 cells from 80–90% confluent monolayer cultures were trypsinized and seeded at a density of 1250 cells per well. The plates were then centrifuged at 1500 rpm for 5 min and incubated at 37 °C in a humidified atmosphere of 5% CO_2. Spheroid growth was monitored daily in a Primovert Inverted ZEISS microscope (objective 4×) with an integrated HD camera, and images were analysed using the free software SpheroidSizer (http://pleiad.rwjms.rutgers.edu/CBII/downloads/SpheroidSizer.zip), a high-throughput MATLAB-based image analysis software. When the spheroids reached diameters in the range of 350–400 μm (typically on day 3), the viability assay was performed.

Cell viability of spheroid cultures. U87 cells were cultured as spheroids for 3 days. Then 100 μL of culture medium were removed from each well and 100 μL of Na[*o*-⁵⁷FESAN] were added to final concentrations of 100 μM, 150 μM and 200 μM, and the spheroids were incubated for 24 h at 37 °C/5% CO_2. As a control, wells were incubated with 100 μL of complete culture medium. Cell viability was evaluated using the CellTiter-Glo® 3D Cell Viability Assay. Briefly, 100 μL were removed from each well and 40 μL of the reagent solution were added. Plates were incubated for 15 min in the dark with agitation at room temperature, after which 100 μL were transferred to a 96-well white-bottom plate and luminescence was determined in a Varioskan LUX Multimode Microplate Reader.

Irradiation of spheroid cultures. U87 spheroids were obtained as described above and incubated with Na[*o*-⁵⁷FESAN] diluted to final concentrations of 100, 150 and 200 μM. As a control, wells were incubated with 100 μL of complete culture medium. After 24 h of incubation, the plates were irradiated with the ⁵⁷Co source (0.4 mGy). Afterwards, the medium was carefully removed, 200 μL of fresh medium were added and a 24 h incubation was performed at 37 °C/5% CO_2. Cell viability was then evaluated using the CellTiter-Glo® 3D Cell Viability Assay as described above. For comparison purposes, spheroids were treated with the same protocol, except for the irradiation step.

Imaging nuclear morphology in U87 cells. U87 cells (*ca.* 10⁵ cells) were seeded into 6-well plates containing a coverslip and allowed to attach overnight. The next day, cells were incubated (or not, as the control) with 50 μM of Na[*o*-⁵⁷FESAN] for 24 h at 37 °C, after which they were irradiated with the ⁵⁷Co source (0.4 mGy, 2 h). Then, the medium was removed, and the cells were washed with PBS before being fixed with 4% formaldehyde for 15 min at room temperature. After washing, cells were mounted in Fluoroshield with DAPI (Sigma-Aldrich) and visualized in a Zeiss Axioplan2 imaging microscope (64× magnification).

Imaging cellular morphological alterations (TEM). U87 cells seeded into 6-well plates at approx. 70% confluence were treated with Na[*o*-⁵⁷Fe-FESAN] at 50 μM for 24 h. After incubation, cells were irradiated with the ⁵⁷Co source (0.4 mGy, 2 h) and processed following a standard procedure described previously.[34]

This journal is © the Partner Organisations 2022

Inorg. Chem. Front., 2022, **9**, 1490–1503 | **1493**

Results

Magnetization and Mössbauer spectroscopy

The magnetization of Na[o-^{57}FESAN] was measured as shown in Fig. 1. From 4 K up to 300 K the magnetization increases, indicating that the magnetic moments gradually align along the magnetic field direction, showing a paramagnetic behaviour. At room temperature, the effective magnetic moment of 2.1μ_B fu^{-1} (2.1μ_B per formula unit, consequently per Fe atom) is consistent with Fe(III) in the low spin state, S = 1/2, which agrees with the already reported data for several ferri-based carboranes[44–46] and corroborates the Mössbauer spectroscopy results.

To estimate the magnetic parameters, the representation of the temperature dependence of the inverse of the magnetic susceptibility, χ, was plotted (inset of Fig. 1) and fitted with the Curie–Weiss expression $\chi = C/(T - \theta)$, where C is the Curie constant, T is the temperature and θ is the Weiss temperature. The small and negative value of θ = −16.7 K suggests weak antiferromagnetic interactions between the unpaired spins of the ions. From the obtained C value, C = 0.392 emu mol^{-1} K^{-1}, the magnetic moment was determined, μ_{eff} = 1.77μ_B fu^{-1}, which is very close to the reported values for several ferrabis (dicarbollides)[44–46] and consistent with its low spin d^5 configuration.

The magnetic contribution of [o-^{57}FESAN]$^-$ present in both U87 and RA cells was determined by testing the temperature dependence of the magnetization under a magnetic field of 1 T, as shown in Fig. 2. Since the cells evidenced a strong diamagnetic response, measurements of a control sample for each type of cell without [o-^{57}FESAN]$^-$were performed under the same temperature and magnetic field conditions to sub-
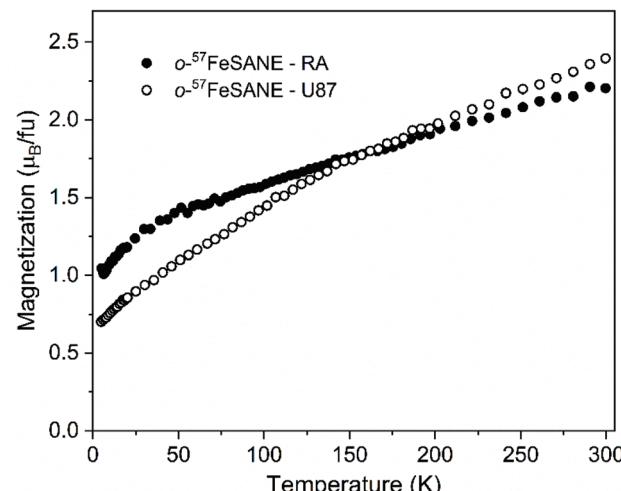

Fig. 2 Temperature dependence of the magnetization under a magnetic field of 1 T of U87 and RA cells loaded with [o-^{57}FESAN]$^-$.

tract the diamagnetism and to determine the paramagnetic signal of the loaded [o-^{57}FESAN]$^-$ in the cells. At room temperature, the magnetic moment reached 2.39 and 2.20μ_B fu^{-1}, for U87 and RA cells, respectively, which were slightly higher than the value obtained for the pristine Na[o-^{57}FESAN]. This reveals not only that [o-^{57}FESAN]$^-$ has entered the cells, but also that a reaction has taken place, increasing the magnetic signal. In addition, the magnetic behaviour of the Fe atoms is preserved as paramagnetic Fe(III) in the low spin state, S = 1/2.

The Mössbauer spectrum of Na[o-^{57}FESAN] is virtually identical to the spectrum of [NMe$_4$][o-FESAN], as reported.[47] The estimated isomer shift (IS) at 80 K in a previous report[47] is given relative to sodium nitroprusside, while in the present study it is given relative to Fe metal. Considering that isomer shifts relative to sodium nitroprusside are 0.26 mm s^{-1} higher than those relative to Fe metal at room temperature,[48] the estimated isomer shift and quadrupole splitting, QS, reported for [NMe$_4$][o-FESAN] are equal within the experimental error to those obtained in the present study for Na[o-^{57}FESAN] (Table 1).

The estimated isomer shifts relative to αFe at 295 K, IS, are within the range of values reported for low-spin Fe^{3+} (S = 1/2), in agreement with magnetization data. The asymmetry of the quadrupole doublet and the broadness of the absorption peaks may be related to slow-spin relaxation of Fe^{3+} or to the
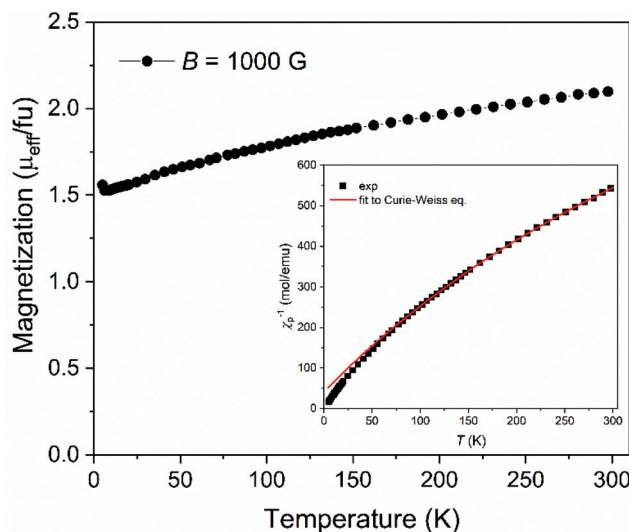
Fig. 1 Magnetic properties of Na[o-^{57}FESAN] powder sample: temperature dependence of the magnetization under a magnetic field of 0.1 T. Inset: temperature dependence of the inverse of the magnetic susceptibility. The solid red line is the fit to the Curie–Weiss law of the experimental data (solid square symbols).

**Table 1** Estimated parameters from the Mössbauer spectra taken at 80 K

Sample	IS (mm s^{-1})	QS (mm s^{-1})
Na[o-^{57}FESAN]	0.26	0.67
U87 cells incubated with ^{57}Fe compound	0.25	1.21

IS, Isomer shift relative to metallic α-Fe at 295 K; QS quadrupole splitting. Estimated errors are ≤0.02 mm s^{-1}.

1494 | *Inorg. Chem. Front.*, 2022, **9**, 1490–1503

This journal is © the Partner Organisations 2022

Gol'danskii Karyagin effect as discussed in detail in [NMe$_4$] [o-FESAN].[47]

The spectrum obtained for the cells incubated with Na[o-^{57}FESAN] consists of a symmetric quadrupole doublet (Fig. 3). The small relative transmission for the cell measurements is due to the very small amount of Fe in the cells. The recoilless factor and consequently the relative transmission do not change significantly between 80 and 4 K. The IS is the same as in Na[o-^{57}FESAN], showing that the electronic state of Fe in the cells is the same as in the starting Na[o-^{57}FESAN].
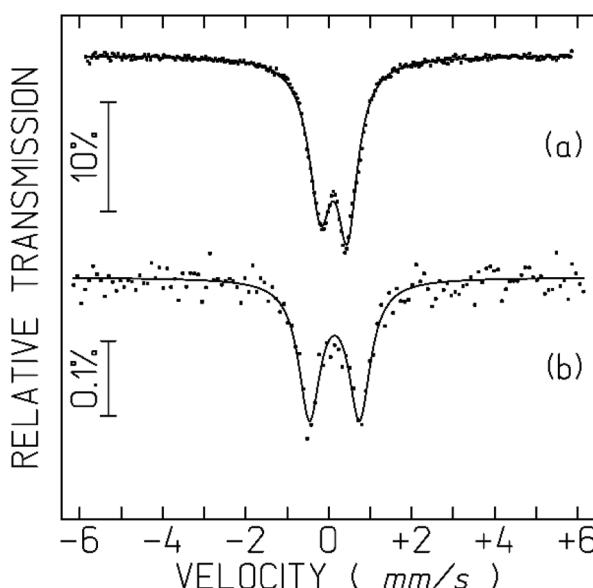
Fig. 3 Mössbauer spectra of Na[o-^{57}FESAN] (a), and the U87 cells incubated with Na[o-^{57}FESAN] (b) taken at 80 K in the solid state. The lines over the experimental points are fitted quadrupole doublets. The estimated parameters are collected in Table 1.

The strong increase in the quadrupole splitting, QS, confirms that the Fe^{3+} environment within the cells is different from [o-^{57}FESAN]$^-$ in the starting Na[o-^{57}FESAN]. This may be related to the fact that [o-FESAN]$^-$ produces intercalative interaction with DNA.[49]

Cytotoxic activity in 2 D cell model

The concentrations of [o-^{57}FESAN]$^-$ for the irradiation studies were previously optimized by calculating the IC$_{50}$ values at 24 h of incubation. The effect of [o-^{57}FESAN]$^-$ on the cellular viability of U87 cells and of RA cells, used as non-tumour, normal glial cells, was evaluated using the MTT assay, and the results are depicted in Fig. 4. As can be seen, the IC$_{50}$ values obtained for both cell lines indicated that, after 24 h of treatment, Na[o-^{57}FESAN] concentrations lower than 100 μM did not induce severe cytotoxic effects and, accordingly, were selected for the subsequent studies with the 2D cell model.

Cellular uptake by PIXE

The radiosensitizing potential of Na[o-^{57}FESAN] could strongly depend on its uptake by the cells. Therefore, studies were carried out to quantify the levels of Fe inside the cells using PIXE and to evaluate any difference in the uptake of [o-^{57}FeSAN]$^-$, between the U87 and RA cells. PIXE is a multi-elemental technique that enables quantification of other elements inside the cells, such as K, Ca, Cu and Zn, and thus gives insights into any imbalance in these physiological elements. The results depicted in Fig. 5 show that the cells loaded with [o-^{57}FESAN]$^-$ present higher Fe levels than the control (non-treated cells) for both cell lines. However, the uptake in the U87 cells is approximately four times higher than that in the RA cells, in either the whole cells or the nuclear fractions.

These results support the entry of [o-^{57}FESAN]$^-$ into the cytoplasm of the cell, reaching the nucleus, which is a particu-

IC$_{50}$ (μM), 24h	
U87	RA
150 ± 23	182 ± 57
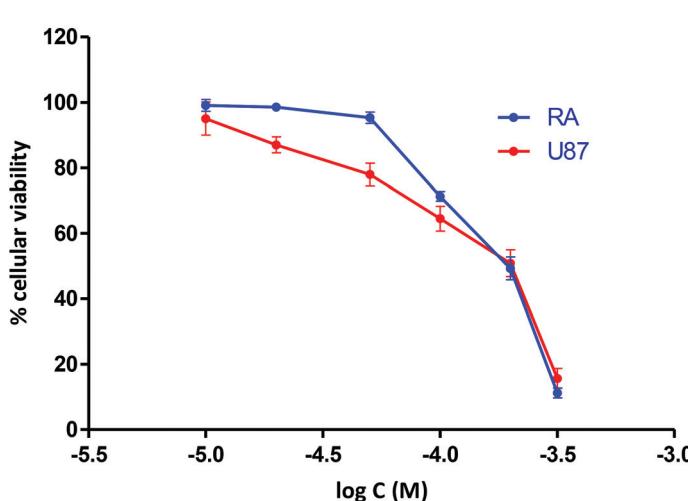
Fig. 4 Cell viability of U87 and RA cells after 24 h exposure to Na[o-^{57}FESAN]. The IC$_{50}$ values were calculated from dose–response curves analysed with the GraphPad Prism software (vs. 5.0).

This journal is © the Partner Organisations 2022

Inorg. Chem. Front., 2022, **9**, 1490–1503 | **1495**
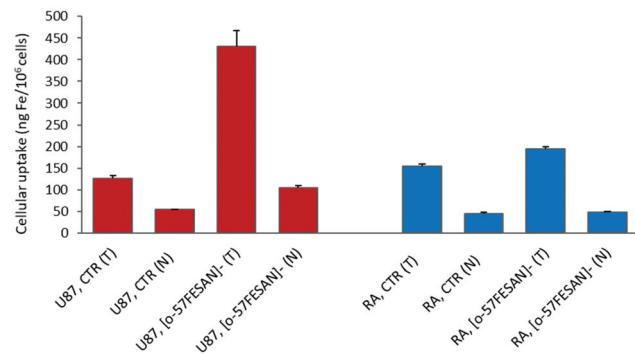
Fig. 5 Concentrations of Fe in U87 and RA whole cell (T) and nuclear (N) fractions after treatment with 50 μM Na[o-^{57}FESAN]. The Fe concentrations in the whole-cell and nuclear for the control cells are also plotted. Values are shown as the mean ± SD.

larly desirable target because the nucleus is the cell's control centre, in which DNA and the transcription machinery reside. Actually, *in silico* studies (Monte Carlo simulations) have shown that the cell-killing effect is more efficient if the energy deposition of the radiation reaction occurs in the nucleus of cells compared with a uniform distribution within the whole cell.[50] To date, only studies related to DNA interaction with Na[o-FESAN] that demonstrate a strong intercalative interaction between Na[o-FESAN] and CT-dsDNA have been reported.[49] The high cellular uptake of small anionic [o-^{57}FESAN]$^-$ molecules by U87 cells and their accumulation in the nucleus (29%) support earlier theoretical results of the effect of the charge and hydrophobicity properties on the translocation of model particles through the nuclear pore complex.[51] The generic hydrophobicity and negative charge of model particles are necessary for their easy translocation through nuclear membranes.[51]

Concerning the relevant physiological elements (see Table S1 at the ESI†), the following data were observed: (i) in both U87 and RA whole cells, the Zn levels increased twice after treatment with Na[o-^{57}FESAN] (in ng per 10^6 cells, U87 controls *vs.* treated, 99 ± 7 and 180 ± 17; RA controls *vs.* treated, 28 ± 2 and 48 ± 3); while (ii) in the respective nuclear fractions an opposite effect was observed for Zn and Ca (in ng per 10^6 cells, U87 control *vs* treated, Zn = 60 ± 2 and 20 ± 2; Ca = 460 ± 10 and 180 ± 4; RA controls *vs.* treated, Zn = 57 ± 4 and 26 ± 2, Ca = 415 ± 8 and 237 ± 4). In treated RA whole cells, K decreased by 40% (controls 2000 ± 100, treated 1125 ± 37). However, in both cell lines, Cu remained essentially unchanged. This observation indicates a similar response of U87 and RA cells towards [o-^{57}FESAN]$^-$. The changes in K, Ca and Zn contents in glial cells may reflect disturbances in the K$^+$ channels involved in the membrane potential, intracellular Ca^{2+} signalling and impaired nuclear activity, after treatment with Na[o-^{57}FESAN]. These changes may have consequences for the level of growth control, cell volume and activity regulation in cancer cells.[52–54] Nevertheless, the interpretation of these results requires further experiments.

Imaging and elemental distribution by nuclear microscopy

The U87 cells that showed a higher uptake towards [o-^{57}FESAN]$^-$ were inspected by nuclear microscopy techniques to visualize the micro distribution of Fe and other physiological elements, such as P, K, Ca and Zn. Fig. 6 depicts representative images of mass density and elemental distributions in U87 cells under the control and 50 μM Na[o-^{57}FESAN] conditions.

The images of mass density showed that U87 control cells are larger with a denser central region, probably corresponding to the nucleus. In treated U87 cells, the density images showed a reduction in the cell size that can translate to a volume decrease.
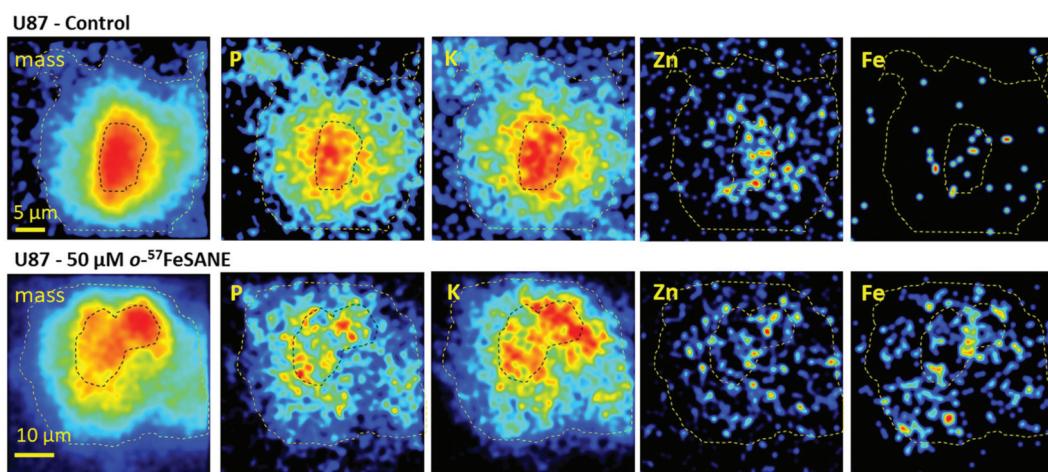
Fig. 6 Mass density (ass) and 2D elemental maps of the distribution of P, K, Zn and Fe in whole U87 cells: control and 50 μM Na[o-^{57}FESAN] treated conditions. The dotted lines indicate the cell contour and the central nuclear region. The mass density and elemental distributions are represented by a colour gradient with a dynamic scale: high level, red, to the low level, dark blue.

The most remarkable difference in the elemental distribution of treated U87 cells was the Fe uniform distribution and its increased content across the whole cells, contrasting with the scattered distribution in the control, as can be observed in Fig. 6. The average Fe concentration in whole control cells was low, below 150 μg per g dry weight, whereas in treated cells a 6-fold increase to 849 + 296 μg per g dry weight was observed. In treated cell peripheral regions and in the denser central nuclear region Fe concentrations did not significantly differ (780 ± 320 *vs.* 950 ± 230 μg per g dry weight). These concentration values are similar to those obtained in the bulk analysis of whole cells and nuclear fractions (concentrations ranging from 600 μg g^{-1} in total cells to 850 μg g^{-1} in the nuclear fraction, on a dry weight basis). Therefore, even for non-toxic concentrations of Na[o-^{57}FESAN], the Fe content in treated cells dramatically increased, which is in line with uptake results. More importantly, Fe does not seem to be compartmentalized in the cell, as its distribution is relatively homogeneous throughout the cell.

The micro distribution of P, K, Ca and Zn in U87 treated cells cannot give a clear definition of cell compartments, contrasting with control cells, where the nuclear region is clearly associated with high contents of P, K and Zn (Fig. 6). In particular, the changes in the microdistribution of Zn reflect those observed in whole cells and nuclear fraction as described above. The rationale behind these elemental fingerprints is the essentiality of the phosphate backbone in the DNA structure,[55] of the K$^+$ cation in chromatin stability (although K$^+$ is mainly a cytoplasm ion)[56] and of Zn as a constituent of protein domains (zinc fingers) and a cofactor of enzymes intrinsically linked to DNA replication machinery.[54] Therefore, the alteration of P, K and Zn compartmentalization in U87 treated cells suggests cellular remodeling after exposure to [o-^{57}FESAN]$^-$ and the subsequent intracellular increase in the Fe concentration.

Evaluation of the Mössbauer irradiation effect

The radiosensitizing potential of [o-^{57}FESAN]$^-$ was evaluated in both cell lines, using the MTT assay before and after Mössbauer irradiation with and without Na[o-^{57}FESAN]. Cells were previously treated with Na[o-^{57}FESAN]$^-$ at 50 and 100 μM followed by 24 h incubation before irradiation. Concerning the non-irradiated cells, no significant cytotoxicity was observed after 24 h of incubation at 50 μM Na[o-^{57}FESAN] for U87 cells, as shown in Fig. 7. The exposure to Mössbauer radiation on the U87 cells incubated with 50 μM Na[o-^{57}FESAN] induced a decrease in cellular viability of about 30% compared with the control (irr) and of about 30% compared with Na[o-^{57}FESAN] (non-irr). At higher doses (100 μM Na[o-^{57}FESAN]), an enhanced radiosensitizing effect was observed for Na[o-^{57}FESAN] (19.7 ± 3.8%), 80% higher compared with the control (irr) and about 60% higher compared with Na[o-^{57}FESAN] (non-irr). For the RA cells, only a slight enhancement of the radiation effect was observed at the same higher dose (100 μM Na[o-^{57}FESAN]), indicating that this effect was rather specific for cancer cells.
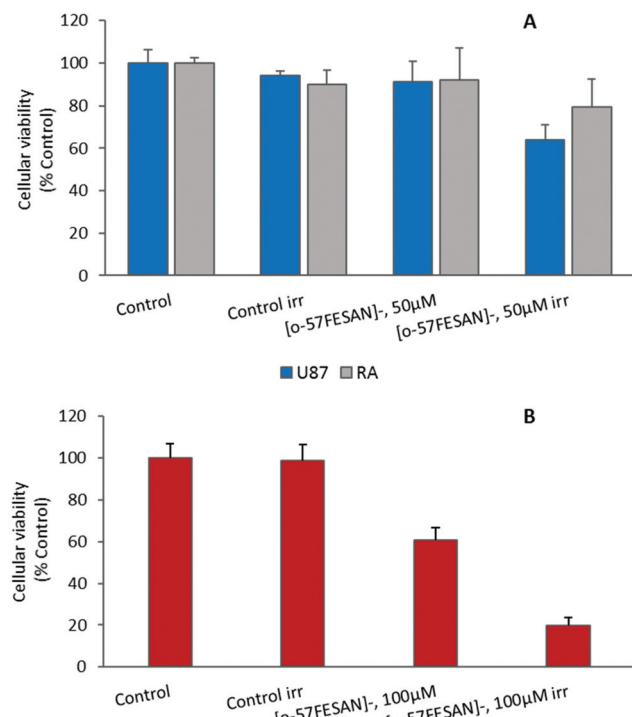
Fig. 7 Cell viability of U87 and RA cells after exposure to Mössbauer irradiation (0.4 mGy, 2 h). (A) U87 (blue colour) and RA (grey colour) cells incubated with Na[o-^{57}FESAN] at 50 μM; (B) U87 cells incubated with Na[o-^{57}FESAN] at 100 μM. Results are shown as the mean ± SD of two independent experiments done with at least six replicates per condition.

Further irradiation studies were also performed as proof-of-concept experiments to confirm that the Mössbauer effect was responsible for the cell death observed. ^{57}Co ($t_{1/2}$ = 272 d) decays by electron capture to the 136.4 keV level in ^{57}Fe, which is de-excited both by 136.4 keV (12.3%) γ rays and by emission of 122 keV (87.5%) and 14.4 keV γ rays (see the decay scheme below). The 122 keV γ rays have a relative probability of 87.5%. Therefore, X-rays at equivalent energy and dose (0.4 mGy) were used to irradiate cells. According to these results (Fig. 8), X-ray irradiation did not induce significant killing of the cells.

Effects of Na[o-^{57}FESAN] in 3D culture models

Cytotoxic activity of Na[o-^{57}FESAN] in 3D models. The cytotoxic activity of Na[o-^{57}FESAN] was further evaluated in more advanced culture models, where tumour cells were grown in a 3D environment, forming spheroids. The concentrations of Na[o-^{57}FESAN] selected to evaluate its cytotoxic activity in spheroid cultures of U87 GBM cells were based on IC$_{50}$ values determined for monolayer cultures, using the MTT assay (around 150 μM for both cell lines), with concentrations one-third below and above these values also being taken into consideration. The viability of the spheroids was studied following a 24 h incubation period, as shown in Fig. 9a, using the CellTiter-Glo® 3D Cell Viability Assay, suitable for advanced culture models. In parallel, the spheroids' growth was also
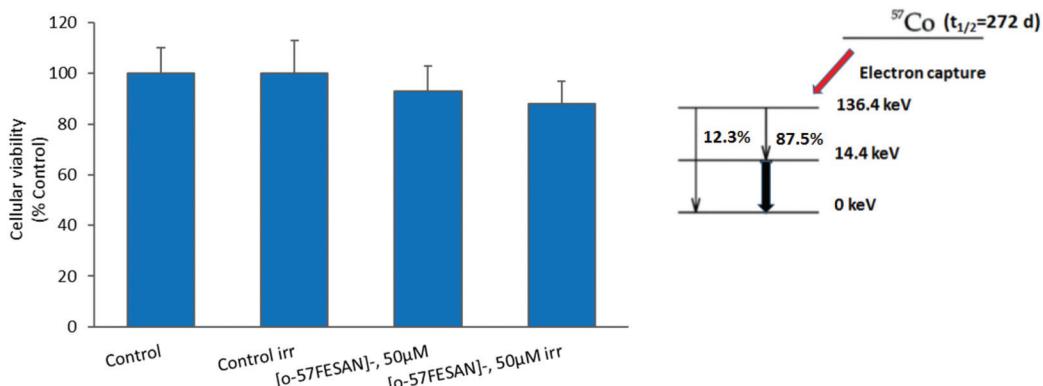
Fig. 8 Cellular viability of U87 GBM cells after irradiation with X-rays in the presence of 50 µM Na[o-^{57}FESAN]. Irradiation was done using a Philips MCN 165 X-ray tube and a YXLON 9421 high-voltage generator at a 0.4 mGy radiation dose. ISO beam quality N120 was used (E_{max} = 120 keV, E_{ave} = 100 keV, filtered with 4 mm Al + 5 mm Cu + 1 mm Sn).
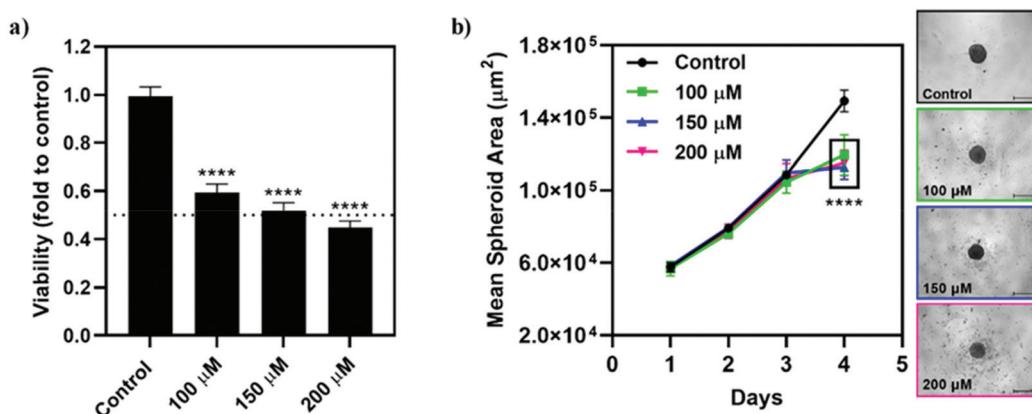
Fig. 9 Effects of the incubation of Na[o-^{57}FESAN] on U87 spheroids. (a) Cellular viability of U87 spheroids at 24 h, assessed using the CellTiter-Glo® 3D Cell Viability Assay, and (b) spheroid growth after incubation with Na[o-^{57}FESAN] at 100, 150 and 200 µM, for 24 h, on day 3, represented by the mean spheroid area (in µm²) as a function of the number of days in culture. Controls consist of spheroids incubated only with the medium. Data are presented as the average ± SEM of 5/6 replicates. Statistical significance was calculated using one-way ANOVA, followed by Dunnett's test comparing treated spheroids with control spheroids (**** $p \leq 0.0001$).

evaluated throughout the culture period, as depicted in Fig. 9b.

Qualitatively, the incubation of the spheroids with Na[o-^{57}FESAN] did not seem to affect the shape and integrity of the spheroids. The circularity of the spheroids was also not severely affected after incubation with Na[o-^{57}FESAN], with the spheroids having maintained regular shapes as reflected by circularity values very close to 1 (data not shown). Quantitatively, the growth and size of the spheroids from the U87 cell line were affected after 24 h of incubation with Na[o-^{57}FESAN] (Fig. 9b), considering that treated spheroids stopped growing after incubation with the compound, which was not observed for spheroids from the control condition.

The viability results obtained (Fig. 9a) reflect an obvious cytotoxic effect of [o-^{57}FESAN]⁻ on the spheroids from U87,

suggesting that [o-^{57}FESAN]⁻ can penetrate in more complex cellular systems, affecting tumour resistance mechanisms.

Based on the importance of this type of metallacarborane compound, we thus foresee that Na[o-^{57}FESAN] could be explored within the scope of a low-dose approach for glioblastoma radiotherapy. In our previous report on metallabis(dicarbollide), Na[o-COSAN], we demonstrated that this type of compound showed no cytotoxicity in normal cells and no acute toxicity in a mouse model.[39] Although the results are preliminary and further studies are needed for the validation of this approach, the present work has lifted the veil on a new type of low-dose radiation glioblastoma therapy with such promising small anionic compounds. Therefore, we consider that the ferrabis(dicarbollide) Na[o-^{57}FESAN] described in this study could constitute a promising approach for radiation therapies, also benefiting from its solubility in water, as

1498 | *Inorg. Chem. Front.,* 2022, **9**, 1490–1503

This journal is © the Partner Organisations 2022

solubility is a main challenge in the development of chemotherapeutic drugs.

Radiosensitizing effect of Na[o-^{57}FESAN] on spheroids

The radiosensitizing effect of [o-^{57}FESAN]$^-$ was further evaluated in spheroid cultures from the tumour cell line, U87, through the CellTiter-Glo® 3D Cell Viability Assay. The concentrations used were chosen based on the IC$_{50}$ values determined for monolayer cultures, using the MTT assay, while concentrations one-third below and above these values were also used, as before. Spheroids were incubated with Na[o-^{57}FESAN] for 24 h, after which they were irradiated and left to recover for an additional 24 h period, followed by the viability assessment (Fig. 10a). In parallel, the spheroids' growth was evaluated throughout the culture period, as depicted in Fig. 10b. As before, the circularity of the spheroids was not severely affected by incubation with Na[o-^{57}FESAN] and irradiation (data not shown).

Spheroids from the tumour cell line stopped growing after being subjected to incubation with Na[o-^{57}FESAN] and Mössbauer irradiation (Fig. 10a). However, the irradiation effect on its own is not significant when comparing irradiated spheroids with spheroids that were not irradiated, both for the control and for the Na[o-^{57}FESAN] treated cells.

The viability results obtained suggest that there is a cytotoxic effect on U87 spheroids that is slightly increased after irradiation (Fig. 10a).
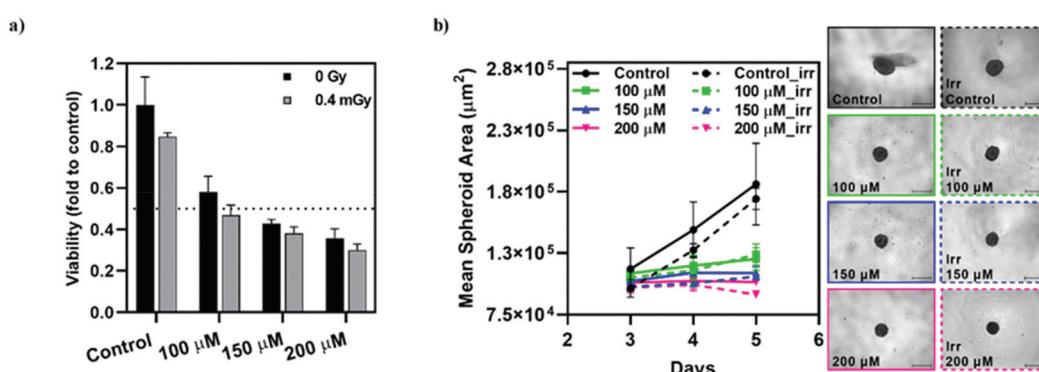
Fig. 10 Radiosensitizing effects of Na[o-^{57}FESAN] on U87 spheroids. (a) Cellular viability of U87 spheroids incubated with Na[o-^{57}FESAN] for 24 h and irradiated, assessed using the CellTiter-Glo® 3D Cell Viability Assay. (b) U87 spheroid growth after incubation with Na[o-^{57}FESAN] at 100, 150 and 200 μM, for 24 h, on day 3, followed by irradiation on day 4 and viability assessment on day 5, represented by the mean spheroid area (in μm^2) as a function of the number of days in culture. Controls consist of spheroids incubated only with the medium. Data are presented as the average $\pm$ SEM of 2 replicates.
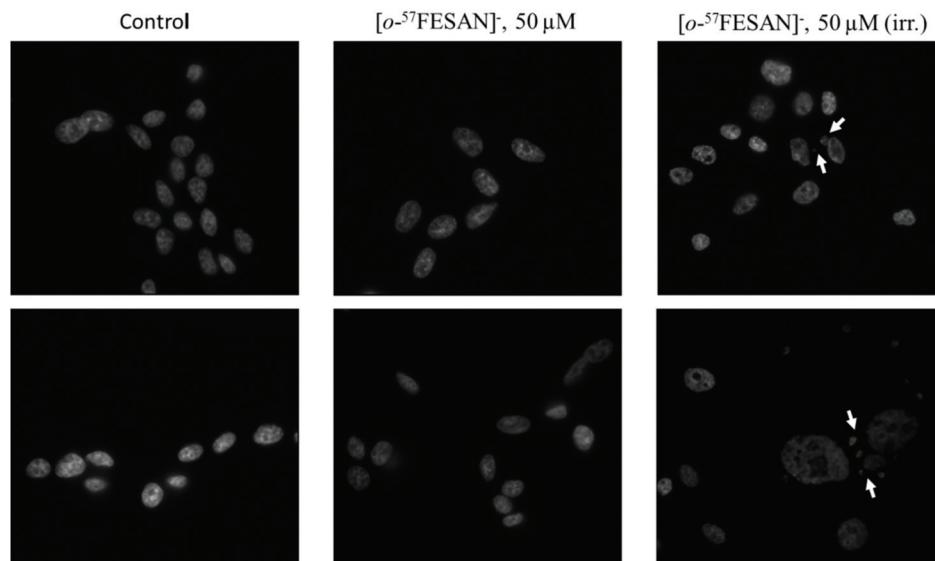
Fig. 11 Fluorescence microscopy for visualizing cellular responses in non-treated cells (control; left panel), 50 μM Na[o-^{57}FESAN]-treated but non-irradiated cell (middle panel), or 50 μM Na[o-^{57}FESAN]-treated cells that were also subjected to Mössbauer irradiation (right panel). Morphological damage to the nucleus was observed as indicated by the presence of nuclear fragments and abnormalities (white arrows).
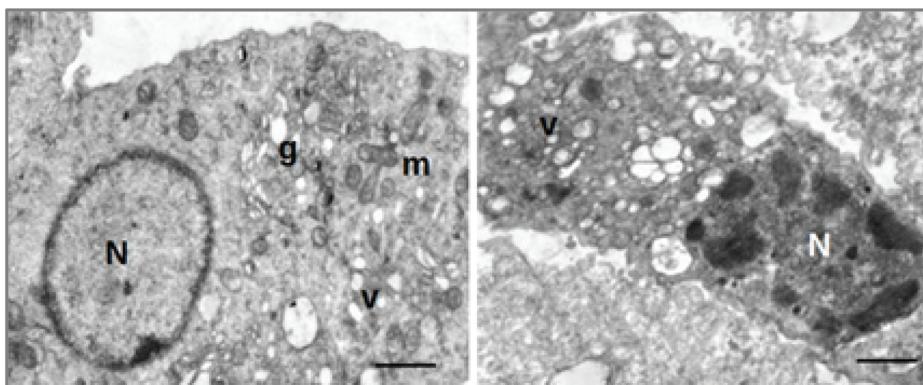
Fig. 12 Thin-section transmission electron microscopy images of U87 cells treated for 24 h with 50 μM [o-^{57}FESAN]$^-$ before and after Mössbauer irradiation (see Experimental section for details). Samples were analyzed and photographed in a JEOL 1200-EX electron microscope. Non-irradiated (left) and irradiated cells (right). N, Nucleus; g, Golgi apparatus; m, mitochondria; v, vacuoles. Bars = 1 micrometer.

Overall, these results suggest that [o-^{57}FESAN]$^-$ exerts a cytotoxic effect that is increased after Mössbauer irradiation, affecting its viability.

Cellular morphological alterations after irradiation

The cellular response to Mössbauer irradiation was evaluated by fluorescence microscopy and transmission electron microscopy (TEM) using the U87 cells. Cellular damage was assessed by incubating the cells with 50 μM Na[o-^{57}FESAN], followed or not by irradiation as described above.

The results obtained using fluorescence microscopy clearly show that there seems to be an increase in the number of nuclear abnormalities and nuclear fragmentation in the samples that had been treated with Na[o-^{57}FESAN] and then subjected to irradiation (Fig. 11), evidencing the toxic effect of this prospective combined treatment modality.

The effects at the cellular organelle level were evaluated using transmission electron microscopy (TEM). This technique enables the visualization of the structural integrity of the cell, providing a spatial resolution that is nearly three orders of magnitude higher than conventional light microscopy, allowing the resolution of structural details in the nanometre range. Electron microscopic study of irradiated cells showed disruption of cellular structures with vacuolization of cytoplasmic membranes and clumping of the chromatin, suggestive of apoptotic phenomena (Fig. 12).

Conclusions

Despite aggressive treatment regimens that include surgery, radiotherapy (RT) and chemotherapy, glioblastoma remains a fatal disease. Treatment failure is mainly ascribed to the tumour location, its high infiltrative capacity that prevents complete tumour ablation and the lack of specificity and efficacy among current chemotherapeutics.

In glioblastoma, the resistance of tumours, as well as toxicity to normal tissues, limits the efficacy of RT. Treatment protocols using low-dose radiation could be more effective, providing local tumour control with minor toxicity to normal tissues. In addition, low-dose radiation could stimulate immune responses, the induction of DNA damage and the occurrence of apoptosis that, all together, might provide effective local tumour control.

One of the goals is to achieve a radiation treatment in which the total dose of radiation is less than that given in standard RT. In low-dose radiation therapy, the total dose may be given in fewer treatments or over a shorter period than standard RT, thus causing less damage to nearby healthy tissue.

Chemotherapy given as an adjuvant to RT or before RT has been widely practiced in patients with glioblastoma. However, such treatments have had limited success.

The present work demonstrates the potential of a low-dose approach for glioblastoma treatment, exploring the Mössbauer effect. The studies confirmed that the Mössbauer effect is responsible for the decrease in cellular viability observed in both 2D and 3D cellular models of the U87 GBM cells. In addition, the radiation effect on GBM cells differed from that of normal glial cells (rat astrocytes). It was found that low doses of radiation in combination with [o-^{57}FESAN]$^-$ at non-toxic concentrations increase the killing effect by 60% in a resonance radiation dose response.

[o-^{57}FESAN]$^-$ enters the cells and distributes randomly through the cells; 29% was found in the nuclear cell fraction. It should be highlighted that the absorption of 14.4 keV photons results in a cascade of secondary radiation such as Auger electrons that seems to be responsible for the cellular damage observed. A single Auger event can be lethal for a cell if generated near to cellular vital structures. Therefore, it is expected that damage to cellular biological structures would be more severe with charged particles (electrons), if generated inside the cell, than with high-energy photons (γ- and X-rays).

The results from this study support the use of low-dose regimens either alone or as an adjuvant for glioblastoma treatment, thus creating new platforms to explore innovative treatment regimens for brain tumours.

1500 | *Inorg. Chem. Front.*, 2022, **9**, 1490–1503

This journal is © the Partner Organisations 2022

Improvements in particle technology, advances in medical imaging and modelling and the fact that new irradiation facilities are becoming available at hospitals make low-doses radiotherapies, such as the Mössbauer effect, a viable choice for cancer medical therapy especially indicated for tumours resistant to chemotherapy and conventional radiotherapy. All of this evidence promises to make the low-dose approach by the Mössbauer effect a cutting-edge technology readily accessible for glioblastoma radiotherapy.

Author contributions

Fernanda Marques and Clara Viñas: Conceived and supervised the study. Ana B. Buades: Synthesis and characterization; Laura C. J. Pereira, Bruno J. C. Vieira, Ana C. Cerdeira, João C. Waerenborgh: Magnetization, Mössbauer spectroscopy and Mössbauer irradiation studies. Teresa Pinheiro: Uptake studies by PIXE and nuclear microscopy. António Matos: Electron microscopy (TEM) studies. Catarina G. Pinto, Joana F. Guerreiro, Filipa Mendes, Fernanda Marques: Biological studies; writing-original draft: Fernanda Marques, Clara Viñas and Francesc Teixidor; discussions of the research, writing-review and editing, all the authors. All authors have read and agreed to the published version of the manuscript.

Conflicts of interest

The authors declare no competing financial interest.

Acknowledgements

References

1 G. Principi, The Mössbauer effect: A romantic scientific page, *Metals*, 2020, **10**, 992.

2 A. Lancok and L. Volfova, Mössbauer spectroscopy: Epoch-making biological and chemical applications, *Pure Appl. Chem.*, 2017, **89**, 461–470.

3 A. A. Kamnev, K. Kovacs, I. V. Alenkina and M. I. Oshtrakh, Mössbauer spectroscopy in biological and biomedical research, in *Mössbauer Spectroscopy: Applications in Chemistry, Biology, and Nanotechnology, 1st edition*, ed. V. K. Sharma, G. Klingelhofer and T. Nishida, John Wiley & Sons, 2013.

4 C. Ueda, M. Langton and M.-E. Pandelia, Characterization of Fe–S clusters in proteins by Mössbauer spectroscopy, *Methods Mol. Biol.*, 2021, **2353**, 281–305.

5 M. E. Pandelia, D. Bykov, R. Izsak, P. Infossi, M. T. Giudici-Orticoni, E. Bill, F. Neese and W. Lubitz, Electronic structure of the unique [4Fe-3S] cluster in O_2-tolerant hydrogenases characterized by ^{57}Fe Mössbauer and EPR spectroscopy, *Proc. Natl. Acad. Sci. U. S. A.*, 2013, **110**, 483–488.

6 M. I. Oshtrakh, Applications of Mössbauer spectroscopy in biomedical research, *Cell Biochem. Biophys.*, 2019, **77**, 15–32.

7 M. Y. Ali, C. R. Oliva, A. S. M. Noman, B. G. Allen, P. C. Goswami, Y. Zakharia, V. Monga, D. R. Spitz, J. M. Buatti and C. E. Griguer, Radioresistance in glioblastoma and the development of radiosensitizers, *Cancers*, 2020, **12**, 2511.

8 E. R. Jamieson and S. J. Lippard, Structure, recognition, and processing of cisplatin–DNA adducts, *Chem. Rev.*, 1999, **99**, 2467–2498.

9 M. Candelaria, A. Garcia-Arias, L. Cetina and A. Dueñas-Gonzalez, Radiosensitizers in cervical cancer. Cisplatin and beyond, *Radiat. Oncol.*, 2006, **1**, 15.

10 C. W. Fong, Platinum based radiochemotherapies: Free radical mechanisms and radiotherapy sensitizers, *Free Radicals Biol. Med.*, 2016, **99**, 99–109.

11 M. R. Gill and K. A. Vallis, Transition metal compounds as cancer radiosensitizers, *Chem. Soc. Rev.*, 2019, **48**, 540–557.

12 R. L. Mills, C. W. Walter, L. Venkataraman, K. Pang and J. J. Farrell, A novel cancer therapy using a Mössbauer-isotope compound, *Nature*, 1988, **336**, 787–789.

13 W. Y. Ma, I. Ortalli, G. Pedrazzi, S. Vaccari and C. Carlo-Stella, Inactivation of bone marrow cultures and K562 leukaemic cell line by Mossbauer effect, *Anticancer Res.*, 1998, **18**, 419–423.

14 C. Fitzmaurice, D. Dicker, A. Pain, H. Hamavid, M. Moradi-Lakeh, M. F. MacIntyre, C. Allen, G. Hansen, R. Woodbrook, C. Wolfe, *et al.*, The global burden of cancer 2013, *Oncology*, 2015, **1**, 505–527.

15 P. Gimenez, H. Elleaume and J.-L. Ravanat, Radiotherapy by photoactivation of iron nanoparticles and Mössbauer effect, in *Medical Applications of Synchrotron Radiation MASR 2015*, Villard de Lans, France, 2015.

16 Y. Xie, Y. Han, X. Zhang, H. Ma, L. Li, R. Yu and H. Liu, Application of new radiosensitizer based on nano-biotechnology in the treatment of glioma, *Front. Oncol.*, 2021, **11**, 633827.

This journal is © the Partner Organisations 2022

Inorg. Chem. Front., 2022, **9**, 1490–1503 | **1501**

17 D. Alberti, N. Protti, A. Toppino, A. Deagostino, S. Lanzardo, S. Bortolussi, S. C. Voena, R. Chiarle, S. G. Crich and S. Aime, A theranostic approach based on the use of a dual boron/Gd agent to improve the efficacy of boron neutron capture therapy in the lung cancer treatment, *Nanomedicine*, 2015, **11**, 741–750.

18 S. Wang, C. Blaha, R. Santos, T. Huynh, T. R. Hayes, D. R. Beckford-Vera, J. E. Blecha, A. S. Hong, M. Fogarty, T. A. Hope, D. R. Raleigh, D. M. Wilson, M. J. Evans, H. F. Van Brocklin, T. Ozawa and R. R. Flavell, Synthesis and initial biological evaluation of boron-containing prostate-specific membrane antigen ligands for treatment of prostate cancer using boron neutron capture therapy, *Mol. Pharmaceutics*, 2019, **16**(9), 3831–3841.

19 M. Couto, C. Alamón, S. Nievas, M. Perona, M. A. Dagrosa, F. Teixidor, P. Cabral, C. Viñas and H. Cerecetto, Bimodal therapeutic agents against glioblastoma, one of the most lethal forms of cancer, *Chem. – Eur. J.*, 2020, **26**, 14335–14340.

20 M. Couto, C. Alamón, M. F. García, M. Kovacs, E. Trias, S. Nievas, E. Pozzi, P. Curotto, S. Thorp, M. A. Dagrosa, F. Teixidor, C. Viñas and H. Cerecetto, Closo-carboranyl- and metallacarboranyl [1,2,3]triazolyl-decorated lapatinib-scaffold for cancer therapy combining tyrosine kinase inhibition and boron neutron capture therapy, *Cells*, 2020, **9**, 1408.

21 D. Alberti, A. Michelotti, A. Lanfranco, N. Protti, S. Altieri, A. Deagostino and S. G. Crich, In vitro and in vivo BNCT investigations using a carborane containing sulfonamide targeting CAIX epitopes on malignant pleural mesothelioma and breast cancer cells, *Sci. Rep.*, 2020, **10**, 19274.

22 E. O. Zargham, C. A. Mason and M. W. Lee Jr., The use of carboranes in cancer drug development, *Int. J. Cancer Clin. Res.*, 2019, **6**, 110.

23 C. Viñas, The uniqueness of boron as a novel challenging element for drugs in pharmacology, medicine and for smart biomaterials, *Future Med. Chem.*, 2013, **5**, 617–619.

24 *Handbook of Boron Science with Applications in Organometallics, Catalysis, Materials and Medicine*, ed. N. S. Hosmane and R. Eagling, World Scientific, London, Vol. 4, Boron in Medicine, 2019; and references therein.

25 G. Calabrese, A. Daou, E. Barbu and J. Tsibouklis, Towards carborane-functionalised structures for the treatment of brain cancer, *Drug Discovery Today*, 2018, **23**(1), 63–75.

26 F. Issa, M. Kassiou and L. M. Rendina, Boron in drug discovery: Carboranes as unique pharmacophores in biologically active compounds, *Chem. Rev.*, 2011, **111**(9), 5701–5722.

27 I. B. Sivaev and V. V. Bregadze, Polyhedral boranes for medical applications: Current status and perspectives, *Eur. J. Inorg. Chem.*, 2009, **11**, 1433–1450.

28 Z. J. Lesnikowski, Recent developments with boron as a platform for novel drug design, *Expert Opin. Drug Discovery*, 2016, **11**(6), 569–578.

29 P. Stockmann, M. Gozzi, R. Kuhnert, M. B. Sárosi and E. Hey-Hawkins, New keys for old locks: Carborane-containing drugs as platforms for mechanism-based therapies, *Chem. Soc. Rev.*, 2019, **48**, 3497–3512.

30 *Boron-Based Compounds: Potential and Emerging Applications in Medicine*, ed. E. Hey-Hawkins and C. Viñas, Wiley, 2018; and references therein.

31 P. Cigler, M. Kozisek, P. Rezacova, J. Brynda, Z. Otwinowski, J. Pokorna, J. Plesek, B. Gruner, L. Doleckova-Maresova, M. Masa, J. Sedlacek, J. Bodem, H. G. Krausslich, V. Kral and J. Konvalinka, From nonpeptide toward noncarbon protease inhibitors: Metallacarboranes as specific and potent inhibitors of HIV protease, *Proc. Natl. Acad. Sci. U. S. A.*, 2005, **102**(43), 15394–15399.

32 K. Bednarska-Szczepaniak, K. Dziedzic-Kocurek, E. Przelazły, J. Stanek and Z. J. Lesnikowski, Intramolecular rotations and electronic states of iron in the iron bis(dicarbollide) complex $Fe[(C_2B_9H_{11})_2]$ studied by a ^{57}Fe nuclear probe and computational methods, *Chem. Commun.*, 2022, **58**, 391–394.

33 A. Verissimo, L. C. Alves, P. Filipe, J. N. Silva, R. Silva, M. D. Ynsa, E. Gontier, P. Moretto, J. Pallon and T. Pinheiro, Nuclear microscopy: a tool for imaging elemental distribution and percutaneous absorption in vivo, *Microsc. Res. Tech.*, 2007, **70**, 302–309.

34 P. Nunes, I. Correia, F. Marques, A. P. Matos, M. M. C. dos Santos, C. G. Azevedo, J. L. Capelo, H. M. Santos, S. Gama, T. Pinheiro, I. Cavaco and J. C. Pessoa, Copper complexes with 1,10-phenanthroline derivatives: Underlying factors affecting their cytotoxicity, *Inorg. Chem.*, 2020, **59**, 9116–9134.

35 C. Viñas, J. Pedrajas, J. Bertran, F. Teixidor, R. Kivekäs and R. Sillanpää, Synthesis of cobaltabis(dicarbollyl) complexes incorporating exocluster SR substituents and the improved synthesis of [3,3′-Co(1-R-2-R′-1,2-C(2)B(9)H(9))(2)](−) Derivatives, *Inorg. Chem.*, 1997, **36**, 2482–2486.

36 M. F. Hawthorne and T. D. Andrews, Carborane analogues of cobalticinium ion, *J. Chem. Soc., Chem. Commun.*, 1965, 443–444.

37 A. B. Buades, V. S. Arderiu, L. Maxwell, M. Amoza, D. Choquesillo-Lazarte, N. Aliaga-Alcalde, C. Vinas, F. Teixidor and E. Ruiz, Slow-spin relaxation of a low-spin S = 1/2 Fe-III carborane complex, *Chem. Commun.*, 2019, **55**(26), 3825–3828.

38 J. C. Waerenborgh, P. Salamakha, O. Sologub, A. P. Gonçalves, C. Cardoso, S. Sério, M. Godinho and M. Almeida, Influence of thermal treatment and crystal growth on the final composition and magnetic properties of the $YFe_xAl_{12 - x}$ ($4 \leq x \leq 4.2$) intermetallics, *Chem. Mater.*, 2000, **12**, 1743–1749.

39 I. Fuentes, T. García-Mendiola, S. Sato, M. Pita, H. Nakamura, E. Lorenzo, F. Teixidor, F. Marques and C. Viñas, Metallacarboranes on the road to anticancer therapies: Cellular uptake, DNA interaction, and biological evaluation of cobaltabisdicarbollide [COSAN]⁻, *Chem. – Eur. J.*, 2018, **24**, 17239–17254.

40 C.-C. Chang, K. Wang, Y. Zhang, D. Chen, B. Fan, C.-H. Hsieh, J. Wang, M.-H. Wu and J. Chen, Mechanical

1502 | *Inorg. Chem. Front.*, 2022, **9**, 1490–1503

This journal is © the Partner Organisations 2022

property characterization of hundreds of single nuclei based on microfluidic constriction channel, *Cytometry*, 2018, **93**, 822–828.

41 C. H. G. Jakob, B. Dominelli, E. M. Hahn, T. O. Berghausen, T. Pinheiro, F. Marques, M. Reich, J. D. G. Correia and F. E. Kühn, Antiproliferative activity of functionalized histidine-derived Au(ɪ) bis-NHC complexes for bioconjugation, *Chem. – Asian J.*, 2020, **15**, 2754–2762.

42 M. A. Barreiros, T. Pinheiro, M. F. Araujo, M. M. Costa, M. Palha and R. C. da Silva, Quality assurance of X-ray spectrometry for chemical analysis, *Spectrochim. Acta, Part B*, 2001, **56**, 2095–2106.

43 http://www.microbeams.co.uk/Products.html; accessed on 30 October 2021.

44 J. M. Forward, D. M. P. Mingos, T. E. Miller, D. J. Williams and Y.-K. Yan, Synthesis and structural characterization of metallacarborane sandwich salts with tetrathiafulvalene (ttf) $[M(C_2B_9H_{11})_2][ttf]$ (M = Cr, Fe, Ni), *J. Organomet. Chem.*, 1994, **467**, 207–216.

45 I. B. Sivaev and V. I. Bregadze, Chemistry of nickel and iron bis(dicarbollides). A review, *J. Organomet. Chem.*, 2000, **614**, 27–36.

46 O. N. Kazheva, G. G. Alexandrov, A. V. Kravchenko, I. B. Sivaev, I. D. Kosenko, I. A. Lobanova, M. Kajňaková, L. I. Buravov, V. I. Bregadze, A. Feher, V. A. Starodub and O. A. Dyachenko, Synthesis, structure, electrical and magnetic properties of $(BEDT-TTF)2[3,3'-Fe(1,2-C_2B_9H_{11})_2]$, *Inorg. Chem. Commun.*, 2012, **15**, 106–108.

47 T. Birchall and I. Drummond, Móssbauer spectroscopy of bis(carbollyl)iron anions and related molecules, *Inorg. Chem.*, 1971, **10**, 399–401.

48 G. K. Shenoy and F. E. Wagner, *Mössbauer Isomer Shifts*, ed. G. K. Shenoy and F. E. Wagner, North Holland, Amsterdam, 1978.

49 T. García-Mendiola, V. Bayon-Pizarro, A. Zaulet, I. Fuentes, F. Pariente, F. Teixidor, C. Viñas and E. Lorenzo, Metallacarboranes as tunable redox potential electrochemical indicators for screening of gene mutation, *Chem. Sci.*, 2016, **7**, 5786–5797.

50 D. Gabel, S. Foster and R. G. Fairchild, The Monte Carlo simulation of the biological effect of the 10B(n, alpha) 7Li reaction in cells and tissue and its implication for boron neutron capture therapy, *Radiat. Res.*, 1987, **111**, 14–25.

51 M. Tagliazucchi, O. Peleg, M. Kröger, Y. Rabin and I. Szleifer, Effect of charge, hydrophobicity, and sequence of nucleoporins on the translocation of model particles through the nuclear pore complex, *Proc. Natl. Acad. Sci. U. S. A.*, 2013, **110**, 3363–3368.

52 F. Brandalise, D. Ratto, R. Leone, F. Olivero, E. Roda, C. A. Locatelli, M. G. Bottone and P. Rossi, Deeper and deeper on the role of BK and Kir4.1 channels in glioblastoma invasiveness: A novel summative mechanism?, *Front. Neurosci.*, 2020, **14**, 595664.

53 I. F. Abdullaev, A. Rudkouskaya, A. A. Mongin and Y.-H. Kuo, Calcium-activated potassium channels BK and IK1 are functionally expressed in human gliomas but do not regulate cell proliferation, *PLoS One*, 2010, **5**, e12304.

54 K. Kluska, J. Adamczyk and A. Krezel, Metal binding properties, stability and reactivity of zinc fingers, *Coord. Chem. Rev.*, 2018, **367**, 18–64.

55 D. L. Morris, Jr., DNA-bound metal ions: recent developments, *Biomol. Concepts*, 2014, **5**, 397–407.

56 A. Allahverdi, Q. Chen, N. Korolev and L. Nordenskiöld, Chromatin compaction under mixed salt conditions: Opposite effects of sodium and potassium ions on nucleosome array folding, *Sci. Rep.*, 2015, **5**, 8512.

This journal is © the Partner Organisations 2022

Inorg. Chem. Front., 2022, **9**, 1490–1503 | **1503**